Phosphorene as a Polysulfide Immobilizer and Catalyst in High-Performance Lithium–Sulfur Batteries

Lu Li, Long Chen, Sankha Mukherjee, Jian Gao, Hao Sun, Zhibo Liu, Xiuliang Ma, Tushar Gupta, Chandra Veer Singh, Wencai Ren,* Hui-Ming Cheng, and Nikhil Koratkar**

As portable electronic devices such as laptops and cellular phones become more feature-intensive, along with the advent of new wearable technologies (such as smart watches and Google glass), it is becoming increasingly important to develop batteries capable of providing higher energy densities.[1,2] Increased gravimetric and volumetric energy density enables batteries to be developed in light-weight and compact formats, which is a pressing need for next-generation electronics and wearable devices. Apart from high energy density, operation at high gravimetric and volumetric power densities is also important for consumer electronics (such as laptops, cell phones, tablet computers, smart watches, etc.) which could potentially be charged within minutes as opposed to an hour with the present-day technology.

From the above discussion, it is clear that next-generation energy storage devices will need significant improvement to keep pace with the needs of customers who are demanding high specific energy, long service life, high power on demand, and quick charging. The above applications impose demands on battery systems that current lithium (Li)-ion cell chemistries are unable to satisfy, either on a performance or cost basis. This has led to intensive research into alternative (high energy density) battery chemistries based on multielectron reactions – one of the most promising of these alternatives is Li-S batteries (which features a two-electron reaction). Li-S batteries offer a maximum theoretical capacity of ≈1675 mAh g^{-1} and energy density of ≈2600 Wh kg^{-1}, which is markedly superior to Li-ion technology.[3] Besides, elemental sulfur is abundant in nature and could facilitate low-cost and environmentally clean batteries. In spite of the above advantages and attractive features, one of the major technical barriers to realization of high performance Li-S batteries is poor cycle stability. Li-S chemistries are typically plagued with problems associated with dissolution of intermediate polysulfides and gradual loss of active sulfur from the cathode into the electrolyte resulting in so called "shuttle" reactions (resulting in rapid capacity fade with charge–discharge cycling and lithium dendrite issues), self-discharge, slow redox reductions, low utilization of sulfur, and poor Coulombic efficiency.[4–7]

Among the family of atomically thin 2D materials, phosphorene (a monolayer of black phosphorus) has special significance since it offers a direct band gap that lies in between the zero gap graphene and various large band gap 2D transitional metal dichalcogenides. Phosphorene is an atomically thin sheet in which each phosphorus atom bonds with three neighboring atoms forming a puckered honeycomb structure.[8] So far the research community has mainly focused on the electronic and optoelectronic applications of phosphorene such as logic transistors and photodetectors.[9–11] The exploration of this unique material in electrochemical energy storage is still very much in its infancy.[12,13] Here, we demonstrate that incorporation of few-layer nanosheets of phosphorene into a porous carbon nanofiber network (cathode matrix) can significantly improve the cycle life of Li-S batteries. After 500 continuous cycles of charge–discharge, the specific capacity of the Li-S battery with phosphorene is retained above 660 mAh g^{-1} with only ≈0.053% capacity decay per cycle, much better than the baseline battery (without phosphorene), which shows ≈0.25% capacity fade per cycle in only 200 cycles under the same test condition. First-principles density functional theory calculations indicate that this improvement is related to phosphorene's ability to immobilize lithium polysulfides. The binding energy of various lithium polysulfides to phosphorene ranges from 1–2.5 eV, which is significantly greater than a carbon hexatom network (≈0.5 eV). Our results also indicate that the presence of phosphorene lowers the polarization, accelerates the redox reaction, and improves sulfur utilization in the battery. To our knowledge, this is the first study that has experimentally demonstrated the development of high performance Li-S batteries enabled using phosphorene nanosheets. We believe this work will give further impetus to the research community to explore the fundamental

L. Li, T. Gupta, Prof. N. Koratkar
Mechanical, Aerospace, and Nuclear Engineering
Rensselaer Polytechnic Institute
Troy, NY 12180, USA
E-mail: koratn@rpi.edu
L. Chen, Z. Liu, Prof. X. Ma, Prof. W. Ren, Prof. H.-M. Cheng
Shenyang National Laboratory for Materials Science
Institute of Metal Research
Chinese Academy of Sciences
72 Wenhua Road, Shenyang 110016, P. R. China
E-mail: wcren@imr.ac.cn
Dr. S. Mukherjee, Prof. C. V. Singh
Department of Mechanical and Industrial Engineering
University of Toronto
Toronto, ON M5S 3G8, Canada
E-mail: chandraveer.singh@utoronto.ca
Dr. J. Gao, Prof. N. Koratkar
Materials Science and Engineering
Rensselaer Polytechnic Institute
Troy, NY 12180, USA
H. Sun, Prof. C. V. Singh
Department of Materials Science and Engineering
University of Toronto
Toronto, ON M5S 3E4, Canada

DOI: 10.1002/adma.201602734

science and applications of phosphorene in the context of electrochemical energy storage.

There are several methods to produce "bulk" black phosphorus, such as using high-energy mechanical ball-milling of red phosphorus, heating toxic white phosphorus under high pressure or transforming white phosphorus in liquid metal.[14–16] However, these strategies are time-consuming, require toxic precursors and complex procedures, which limit their practicality for large-scale production. Here, we have chosen a green, safe, and efficient mineralizer-assisted gas-phase transformation method to produce high-purity bulk black phosphorus. This method is described in detail in our previous work.[13] Scanning electron microscope (SEM) image (Figure S1a, Supporting Information) shows the morphology of a typical ≈4 mm sized black phosphorus bulk crystal produced by this method. The corresponding energy dispersive X-ray spectrometer (EDS) spectrum is shown in Figure S1b (Supporting Information), indicating that only the elemental P peak is present without any impurities. The X-ray diffraction (XRD) (Figure S1c, Supporting Information) pattern further confirms that these bulk black phosphorus flakes exhibit high crystallinity and match well with the orthorhombic phase showing the (020), (040), and (060) diffraction peaks at $2\theta = 16.90°$, 34.17°, and 52.32°, respectively (JCPDS 76–1957).

We used a liquid exfoliation approach to exfoliate these bulk black phosphorus crystals in *N*-Methyl-2-pyrrolidone (NMP) to obtain few-layer phosphorene nanosheets (FLP). To confirm the morphology and structure of FLP, transmission electron microscopy (TEM), atomic force microscopy (AFM), XRD, and Raman spectroscopy were carried out. As shown in **Figure 1**a, TEM indicates that the size of these nanosheets is 1–2 µm with very small thickness (also confirmed by AFM). The uniformity of size distribution was further verified under an optical microscope (Figure S2, Supporting Information). The measured electron diffraction pattern with sharp diffraction spots is shown in Figure 1b, indicating the highly crystalline orthogonally symmetric structure of FLP. Lattice fringes (Figure 1c) indicate a perfect atomic structure without any visible defects. The measured lattice constants are 3.26 and 4.44 Å, which are consistent with those of black phosphorus.[17] AFM measurement (Figure 1d) indicates that the thickness of these smooth FLP nanosheets lies in the range of 5–10 nm, corresponding to ≈10–20 layers of phosphorene (adjacent layer spacing is ≈0.53 nm). The sharp XRD pattern of FLP (Figure 1e) confirms that the liquid exfoliation process did not change the crystallinity of the phosphorene nanosheets. Compared with the XRD pattern of bulk black phosphorus (Figure S1c, Supporting Information), many small peaks appear in Figure 1e, indicating that these phosphorene nanosheets become less preferentially orientated after liquid exfoliation in NMP. The characteristic A_g^1, B_{2g}, and A_g^2 Raman modes are observed at 361, 438, and 466 cm^{-1} in Figure 1f, respectively, which are in good agreement with previously reported results of few-layer phosphorene.[18,19] These sharp modes further confirm the orthorhombic crystalline structure of FLP. The A_g^1/A_g^2 ratio is greater than 0.6, which indicates that there is no significant oxidation during the exfoliation process.[20]

The cathode in a Li-S battery is typically a porous carbon electrode with entrapped S.[21,22] In this work, we explored the use of a carbon nanofiber (CNF) network that serves as the cathode matrix. To incorporate FLP into the CNF, we directly added commercially available CNF into the FLP-NMP dispersion (Figure S3a, Supporting Information) by the ultrasonic approach. The flexible FLP-CNF membrane was extracted from the dispersion by vacuum filtration (Figure S3b, Supporting Information). The mass fraction of FLP in the electrode matrix was maintained at ≈15%. As indicated in **Figure 2**a–c, the FLP are well dispersed in the 3D CNF network. This was

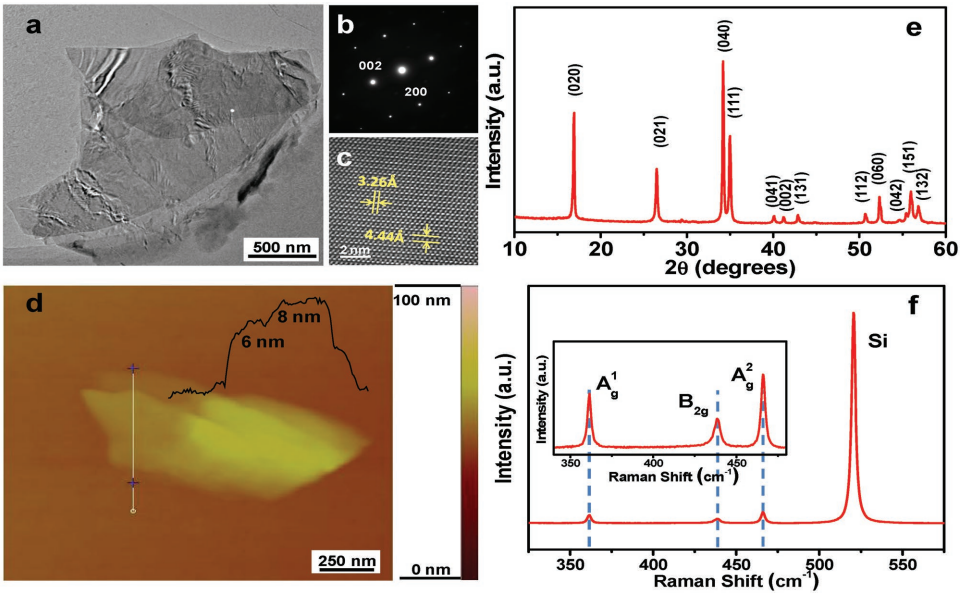

Figure 1. Characterization of few-layer phosphorene (FLP). a) TEM images of FLP exfoliated in *N*-Methyl-2-pyrrolidone. b) Corresponding electron diffraction pattern of FLP (the zone axis is along the [010] direction). c) High-resolution TEM image. d) AFM images, e) XRD pattern, and f) Raman spectra of exfoliated FLP.

Adv. Mater. **2016**,
DOI: 10.1002/adma.201602734

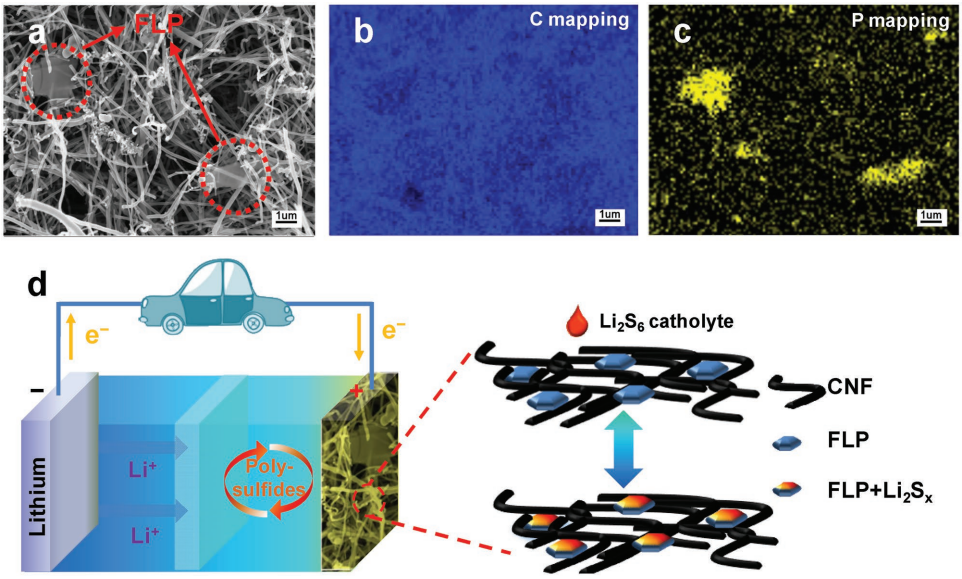

Figure 2. Morphology and microstructure of few-layer phosphorene and carbon nanofiber (FLP-CNF) electrode and schematic diagram of the Li-S battery. a) SEM of FLP-CNF. The FLP sheets are circled by red dotted line for clarity. b) EDS elemental carbon mapping and c) EDS elemental phosphorus mapping in (a). d) Schematic of the FLP-CNF matrix used as the host for the lithium polysulphide catholyte.

also verified by cross-section imaging of the FLP-CNF electrode (Figures S4, S5, Supporting Information). It should be noted that the FLP that decorate the CNF are still transparent (Figure 2a), which indicates that the vacuum filtration process did not cause the phosphorene nanosheets to agglomerate. EDS spectrum of the flexible FLP-CNF membrane (Figure S3c, Supporting Information) shows only the elemental "C" and "P" peaks without any impurities. The phosphorus mapping in Figure 2c and Figures S4,S5 (Supporting Information) confirms that the FLP are uniformly distributed in the CNF network. Figure S6 (Supporting Information) shows additional SEM images of the FLP dispersed in the CNF network. The as-prepared FLP-CNF membrane was then cut and used as the host for dissolved lithium polysulphides, which serve as the active materials that react with Li. The sulfur loading in the FLP-CNF and CNF electrodes was ≈3.3 mg cm^{-2}. A concept schematic of a Li-S battery with polysulfides (bound to the FLP-CNF network) is illustrated in Figure 2d.

We utilized cyclic voltammetry (CV) to investigate the electrochemical reaction kinetics. The CV tests were performed in the coin cell format with polysulfide solution (Li_2S_6, as the active material) added to CNF and FLP-CNF. As shown in **Figure 3**a, there are two pairs of distinct and stable redox peaks for the FLP-CNF electrode, in which the reduction peak (2.40–2.25 V) and the corresponding oxidation peak (2.38–2.50 V) belong to the transition between sulfur (S_8) and high-order lithium polysulfides (Li_2S_x, $4 \leq x \leq 8$), while the cathodic peak (2.07–1.96 V) and the backward oxidation peak (2.27–2.38 V) correspond to the transformation between the high-order lithium polysulfides and Li_2S_2/Li_2S, respectively.[23] A similar CV study on the pure CNF electrode (without FLP) indicates (see Figure 3b) that the redox peaks are deformed and widened (with decreased integral areas), which suggests a sluggish kinetic process. Comparing the peak potentials (Figure 3c) during the redox reactions, it is evident that the FLP-CNF electrode shows higher reduction potential and lower oxidation potential than the baseline CNF, indicating that the FLP significantly lowers the electrode polarization. This can be attributed to the catalysis effect of FLP on the oxidation/reduction of S/Li_2S.[24] Analysis of the onset potentials (Figure 3d, defined as the potentials at which ≈10% of the current value at the peak potential is reached[25]) provides further evidence that the FLP accelerate the redox processes in the Li-S battery system. The onset potential of the FLP-CNF electrode in the oxidation reaction is ≈2.27 V, compared with ≈2.34 V for the pure CNF. With respect to the reduction reaction, the onset potentials for FLP-CNF are ≈2.4 and ≈2.07 V, compared with ≈2.38 and ≈2.05 V for the pure CNF electrode, which are lower by ≈20 mV. These results demonstrate that by coating FLP onto an electrically conductive CNF scaffold, the redox kinetics are accelerated and the polarization losses are also significantly reduced for the Li-S battery.

We carried out galvanostatic charge/discharge tests in the coin cell format to evaluate the Li-S battery performance. For the control, we used a pristine CNF electrode into which we added polysulfide solution (Li_2S_6) forming the baseline electrode. The same amount of polysulfides (as for the control sample without FLP) was also added as the active material to the FLP-CNF electrode. Galvanostatic charge/discharge cycling of Li-S cells with FLP-CNF and CNF cathodes and Li metal as the counter-electrode was carried out. A specific capacity (**Figure 4**a) of 1262, 1092, 1027, 985, 865, and 785 mAh g^{-1} was obtained at 0.2C, 0.5C, 0.8C, 1C, 2C, and 3C rates (1C = 1675 mA g^{-1}), respectively, indicating reversible charge/discharge over a wide range of operating current density. When the rate was restored to 1C after high current density testing, the specific capacity of the FLP-CNF electrode reverts to ≈967 mAh g^{-1}, which is close to the initial value (985 mAh g^{-1}) at 1C current density, indicating good reversibility. By contrast, the initial average discharge capacity of the pure CNF electrode (Figure 4a) is only 944 mAh g^{-1}, which is ≈300 mAh g^{-1} lower than the FLP-CNF

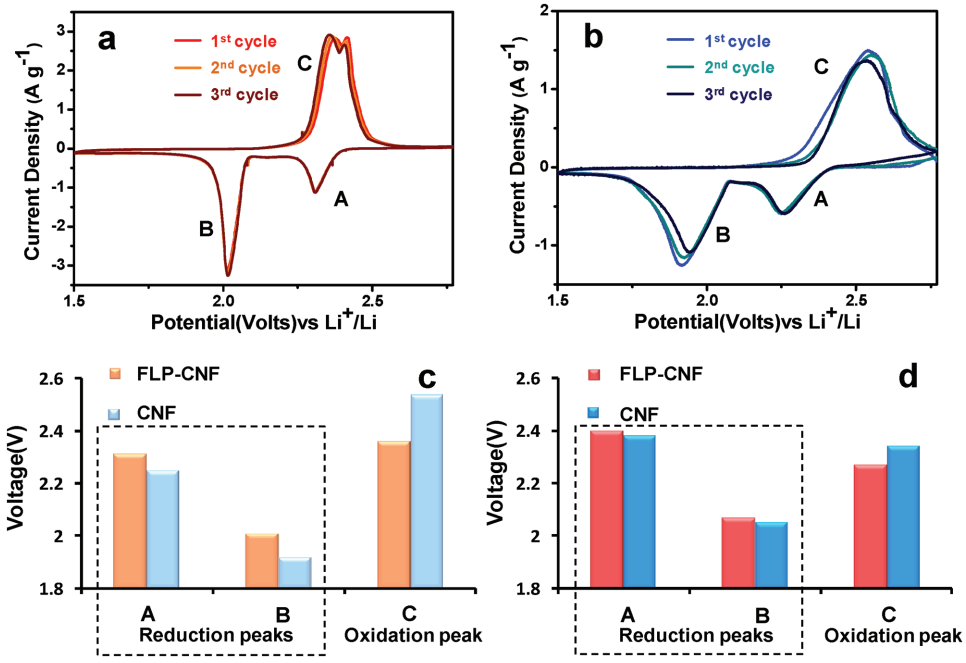

Figure 3. Kinetics of electrochemical reactions in Li-S batteries. CV test of a) FLP-CNF and b) pure CNF electrode. Corresponding c) peak potentials and d) onset potentials of the FLP-CNF and pure CNF electrodes from the second CV cycle in (a) and (b).

battery, indicating significant dissolution and loss of lithium polysulfides into the electrolyte during the initial cycles.[26]

Charge and discharge voltage profiles of the Li-S batteries with FLP-CNF electrode and pure CNF electrode at 0.2 C rate within a potential window of 1.5–2.8 V versus Li^+/Li are presented in Figure 4b. Plateaus in the charge curves stand for the conversion from lithium sulfides to sulfur while plateaus in the discharge curves represent the reduction of sulfur to high-order lithium polysulfides (Li_2S_x, $4 \leq x \leq 8$) at ≈2.3–2.4 V and to the formation of Li_2S_2/Li_2S at ≈2.1 V.[27] From Figure 4b, it is evident that the specific capacity (from the plateau at ≈2.3–2.4 V of discharge curve) of the FLP-CNF electrode is much larger than that of the pure CNF electrode. This is a typical signal that polysulfides dissolution is significantly inhibited and polysulfides have been confined in the cathode zone,[28] which is in consistency with the ex situ adsorption measurement presented later in **Figure 5**g. Additionally, a relatively low polarization value of ≈170 mV at 0.2 C was observed between charge and discharge curves in the FLP-CNF electrode, much lower than the value of ≈250 mV for the pure CNF electrode. Lower polarization is indicative of enhanced electrochemical reaction dynamics in the Li-S battery.[29] By comparing the charge and discharge voltage profiles at different current densities (see Figure S7, Supporting Information), plateaus in charge or discharge processes shift obviously in the case of the pure CNF electrode at high current rates, which indicates that large polarization and slow redox reaction kinetics are the limiting factor for high rate operation. By contrast, as shown in Figure S7 (Supporting Information), the FLP-CNF system displays markedly better performance at high C-rates as compared to the baseline CNF electrode. These results are consistent with the CV results in Figure 3, and illustrate the catalytic effect of FLP in Li-S batteries. Similar results were also obtained for even higher sulfur mass loadings of up to ≈5 mg cm^{-2} in the FLP-CNF electrode (see Figure S8, Supporting Information).

Figure 4c shows the long-term cycling performance of FLP-CNF and pure CNF electrodes at a current density of 1 C. After 500 cycles, the specific capacity of the FLP-CNF electrode is retained above 660 mA h g^{-1} with only 0.053% average capacity decay per cycle. In contrast to this, the average capacity decay per cycle for the pure CNF electrode is about 0.25% over 200 cycles, much higher than the FLP-CNF electrode. The average coulombic efficiency of FLP-CNF is ≈98% as compared to ≈94% for the pure CNF electrode. The decay rate versus cycle index is plotted in Figure S9 (Supporting Information) and indicates large cycle-to-cycle fluctuation for the baseline CNF electrode when compared to the FLP-CNT system, indicating that the presence of FLP improves the electrochemical stability of the Li-S battery. Based on the theoretical capacity of sulfur, the sulfur utilization (Figure 4c inset) for the FLP-CNF reaches ≈57%, which is much greater than the baseline CNF electrode (≈41%). In Figure 4d,e, we have separated out and plotted the high plateau and the low plateau capacity contributions to the total discharge capacity (Figure 4b) for the FLP-CNF and pure CNF systems. The high plateau capacity (Figure 4d) for the FLP-CNF is much greater compared to CNF, which confirms the suppression of polysulfide diffusion in the FLP-CNF. We also find that the low plateau capacity (corresponding to conversion from polysulfides to lithium sulfide) for the FLP-CNF is more stable (Figure 4e) than CNF which is also indicative of polysulfide immobilization. As a final piece of evidence, the discharge voltage plateaus (Figure S10a,b, Supporting Information) are fairly stable over 500 cycles for the FLP-CNF electrode. By contrast, the high/low discharge plateau voltages drop significantly for the baseline CNF electrode in only 200 cycles (Figure S10a,b, Supporting Information). All the above

Adv. Mater. **2016**,
DOI: 10.1002/adma.201602734

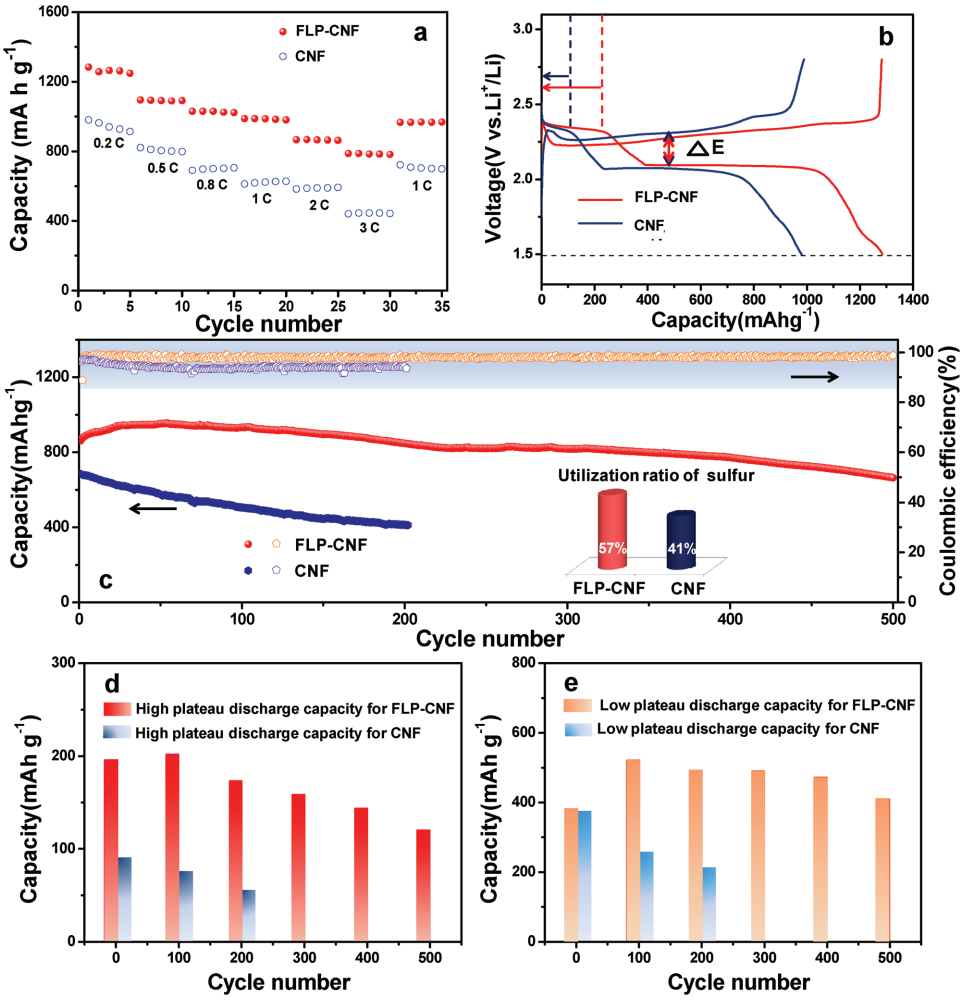

Figure 4. Electrochemical performance of Li-S batteries with FLP-CNF electrode and pure CNF electrode. a) Rate properties at different current densities (1C = 1675 mA g^{-1}). b) Galvanostatic charge–discharge voltage profiles of the first cycle at 0.2 C. c) Cycling stability and coulombic efficiency. Inset shows utilization of sulfur at a current density of 1C (calculated based on the maximum capacity during the cycling, theoretical capacity is 1675 mAh g^{-1}). d) High plateau and e) low plateau discharge capacity for FLP-CNF and pure CNF electrodes from (c).

electrochemical evidence indicates that FLP additives are highly effective as polysulfide immobilizers and electrocatalysts in Li-S batteries.

To understand the underlying mechanisms responsible for the improved Li-S battery performance, we carried out first principles calculations to study the binding energy and changes to the charge density on the phosphorene surface after reacting with a variety of lithium polysulfides. More specifically, we used density functional theory calculations with corrections for van der Walls forces (DFTD) to examine the binding strength of lithium polysulfides to phosphorene surfaces. The monolayer phosphorene structure consists of four P atoms in a unit cell, which are stacked in puckered subplanes (Figure S11, Supporting Information). The calculated charge density plots for Li_2S_x molecules with monolayer phosphorene are shown in Figure 5a–e. The following can be inferred from the charge density contours: (a) as the Li_2S and Li_2S_2 molecules are adsorbed by the phosphorene, strong bonds are formed between S and P atoms (bond lengths 2.18 and 2.12 Å respectively), additionally strong electrostatic interactions are generated between Li and P atoms; (b) however similar interactions between S-P atoms are absent for the larger molecules (such as Li_2S_3, Li_2S_4, Li_2S_6), where the binding is dictated solely by the electrostatic interactions between Li and P atoms; (c) in general, we find that the energies associated with the binding of Li_2S_x species onto phosphorene are larger than the energy increase by individual Li_2S_x molecules forming larger clusters.[30] Therefore, the Li_2S_x compounds have a natural tendency to get adsorbed to the phosphorene surface rather than forming larger clusters. As indicated in Figure 5f, the binding energies of Li_2S, Li_2S_2, Li_2S_3, Li_2S_4, and Li_2S_6 systems over the phosphorene surface were estimated to be 2.49, 1.94, 1.3, 0.93, and 0.92 eV, respectively, which are much higher when compared with the corresponding binding energies on a carbon hexatomic ring network (≈0.5 eV).[31] This implies that phosphorene surfaces are significantly more effective in adsorbing and trapping polysulfides than traditional carbon-based surfaces.

In order to further evaluate the adsorption ability of lithium polysulfides on the surface of phosphorene, ex situ adsorption

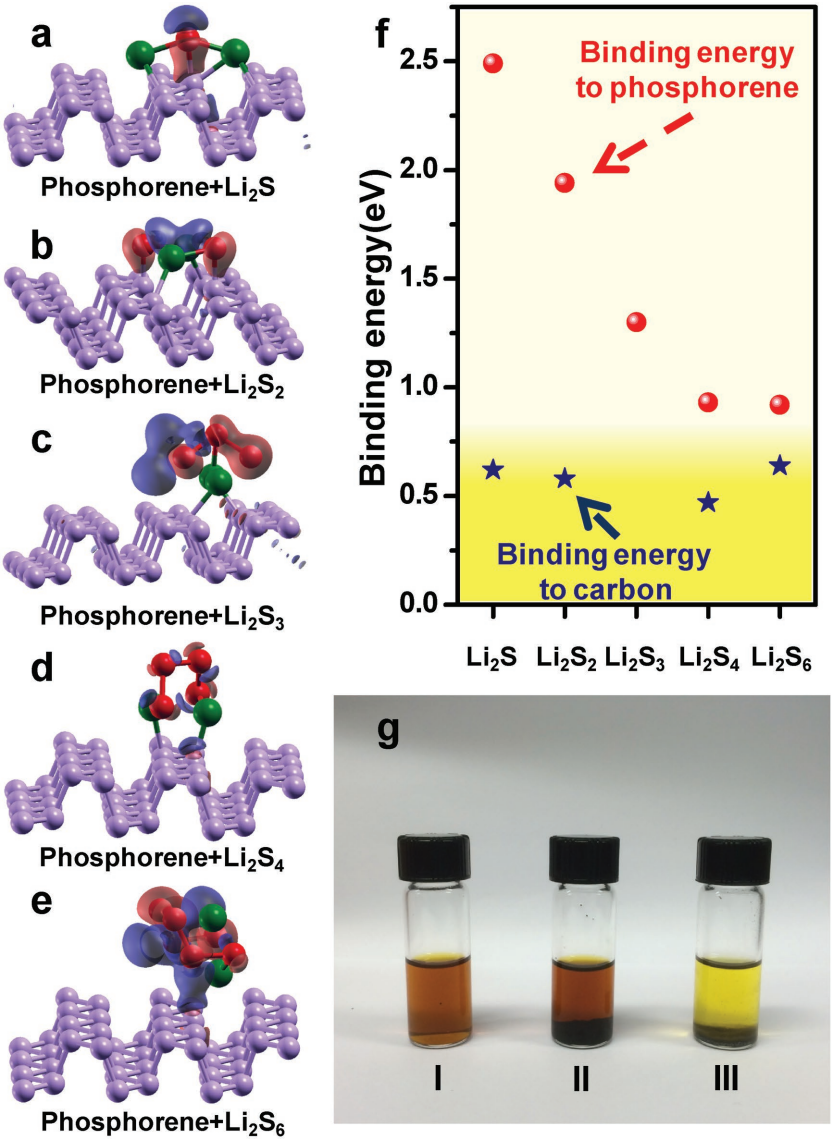

Figure 5. Theoretical calculations and experimental results of lithium polysulfide adsorption. a–e) Atom positions and charge density plot with iso-contour for lithium polysulfide molecule interaction with monolayer phosphorene. Here red, green, and violet spheres represent sulfur, lithium, and phosphorus atoms, respectively. The positive iso-surface in the charge density plot is rendered in red, while negative is in blue. f) Plot of DFT calculated binding energy between lithium polysulfides and phosphorene (red), and carbon hexatomic ring network[31] (blue, the binding energies on the carbon hexatomic ring network include the van der Waals interaction in the simulation). g) Ex situ adsorption measurement (I: pure Li_2S_6; II: Li_2S_6+CNF; III: Li_2S_6+ black phosphorus).

measurements were carried out as shown in Figure 5g. For this test, 5 mmol L^{-1} Li_2S_6 solution (2 mL) was used as a reference. Then pure carbon nanofiber powder and black phosphorus powder were immersed into Li_2S_6 solution for 12 h, and the color change was recorded. Black phosphorus powder could strongly adsorb lithium polysulfides, and the color of dissolved Li_2S_6 solution fades greatly, while the CNF has no observable adsorption on the polysulfide solution since the color of the solution remains the same. This is remarkable considering that for this test the surface area of black phosphorus powder in the vessel is ≈10 times lower (based on Brunauer–Emmett–Teller surface area measurements) than that of the CNF powder. This test, though qualitative in nature, supports our galvanostatic charge–discharge cycling results and theoretical calculations and provides compelling evidence that lithium polysulfides show strong affinity to phosphorene surfaces.

Enhanced binding of polysulfides to the FLP-CNF was also corroborated by post-cycling imaging of the FLP-CNF and pure CNF electrodes. After 100 cycles at a charge/discharge rate of 1C, the morphologies of FLP-CNF electrode are shown in Figure S12b,c (Supporting Information) and the pure CNF electrode are shown in Figure S12d,e (Supporting Information). In Figure S12c (Supporting Information), the contrast of FLP change from transparent to white, suggesting that the FLP has absorbed the polysulfide species. Further, no large aggregations are observed on the FLP-CNF (Figure S12b,c, Supporting Information) in contrast to the baseline CNF (Figure S12d,e, Supporting Information) which shows large deposits. This confirms reduced dissolution loss of polysulphides into the electrolyte and less redeposition onto the FLP-CNF electrode.[32] Post cycling imaging of the Li counter-electrode was also performed. From the cycled anode (Li) morphologies shown in Figure S13 (Supporting Information), the surface of Li anode metal (Figure S13a, Supporting Information), with FLP-CNF as cathode, is much smoother (with less deposition) than that of lithium metal (Figure S13b, Supporting Information), which uses pure CNF as cathode. This result also points to less polysulfide diffusion losses in the FLP-CNF case.

It is important to bench-mark the performance of FLP to other polysulfide immobilizers that have been reported in the literature. We have compared in Figure S14 (Supporting Information) the average capacity decay rate per cycle from some important studies[33–39] with Li-S batteries to the FLP data. The y-axis in Figure S14 (Supporting Information) is the average capacity fade rate per cycle, while the x-axis shows the weight fraction of the polysulfide immobilizer compared to the S (or Li_2S) weight. We also specify on the plot the number of charge/discharge cycles over which the data are averaged and the S loading. It is clear from the plot that FLP offers one of the best performances in terms of lowering the capacity decay rate. Although the weight fraction of FLP additives is only ≈10% of the sulfur weight, its impact is impressive (Figure S14, Supporting Information). One reason for this is that the FLP density (≈2.69 g cm^{-3}) is much lower

Adv. Mater. **2016**,
DOI: 10.1002/adma.201602734

than most polysulfide immobilizers such as metal oxides (CaO: 3.35 g cm^{-3}), sulfides (TiS_2: 3.22 g cm^{-3}), and nitrides (TiN: 5.4 g cm^{-3}). Therefore for the same weight fraction of immobilizer, the active surface area for the phosphorene immobilizer will exceed that of typical metal oxides, sulfides, and nitrides. Moreover, the 2D (sheet) geometry of phosphorene also contributes significantly to achieving greater exposed surface area for polysulfide immobilization. Since lithium polysulfides exhibit strong affinity for phosphorene (Figure 5), maximizing the surface area of the absorbent in the electrode is highly beneficial. Another contributory factor is conductivity; we measured the electrical conductivity of FLP to be ≈450 S m^{-1}, which is higher than what is reported for metal oxides and carbon nitride.[36,37] Electrochemical reaction kinetics of the Li-S battery would therefore be improved due to the higher conductivity of FLP. All of the above factors contribute to the effectiveness of phosphorene as a polysulfide absorbent in Li-S batteries. A preliminary cost analysis for FLP synthesis is also provided in the Supporting Information. At the lab scale, the cost of FLP manufacturing is estimated at ≈$6.6 per gram. We expect that this cost will decrease significantly with Economies of Scale as much larger quantities of raw materials are utilized for industrial-scale production.

To conclude, we show that phosphorene has significant potential as an electrocatalyst and polysulfide immobilizer in Li-S batteries. The ability to trap polysulfides endows phosphorene with an impressive ability to prolong the cycle life of Li-S cells. Our results also indicate that the presence of phosphorene lowers the polarization, accelerates the redox reaction, and improves sulfur utilization in the battery. While electronic and optoelectronic device applications have so far dominated the study of phosphorene, it is our hope that this study will give fresh impetus to the research community to explore the fundamental science and applications of phosphorene in the context of electrochemical energy storage and catalysis.

Experimental Section

Synthesis of Bulk Black Phosphorus: A modified mineralizer-assisted gas-phase transformation method was used to produce high-purity bulk black phosphorus as reported previously.[13] First, red phosphorus (≈1.5 g), AuSn alloy (≈600 mg), and SnI_4 (≈30 mg) were uniformly mixed and vacuum sealed in a quartz ampoule (≈15 cm in length and ≈16 mm in diameter). Then, the sealed ampoule was located in the middle of a tube furnace (Lindberg Blue M (TF55035KC-1) and heated to ≈650 °C within ≈30 min. After maintaining the reaction at ≈650 °C for ≈2 h, the temperature was reduced to ≈500 °C in ≈1 h. This temperature was held for ≈30 min and then the ampoule was cooled down to room temperature. Finally, the formed black phosphorus crystals were taken out and purified by washing in hot acetone.

Synthesis of Few-Layer Phosphorene: 400 mg black phosphorous bulk was added to 80 mL NMP. Tip sonication (Sonics Vibra-cell VC 750 tip sonicator, frequency ≈20 kHz and at 30% power for 3–5 h) was used to exfoliate black phosphorous bulk. After 8–12 h of settling, the dispersion was centrifuged at a rate of ≈1000 rpm for ≈30 min to remove the remaining bulk black phosphorous.

Synthesis of Electrodes: Commercial carbon nanofiber powder was added into NMP solution containing few-layer phosphorene nanosheets. This mixture was ultrasonicated for ≈1–2 h, and then collected by vacuum filtration. After drying at ≈70 °C for ≈1–3 h in vacuum, the electrode was peeled off from the filter membrane. The mass fraction of phosphorene in the composite electrode was ≈15%. The pure carbon nanofiber electrode was fabricated by dispersing commercial carbon nanofiber powder into the pure NMP followed by the same process.

Li-S Battery Measurements: 2032-type coin cells were used to assemble test cells with lithium metals as the counter/reference electrode and Celgard 2340 polypropylene membrane was used as the separator. ≈10 µL of 1 M lithium polysulfide (Li_2S_6) catholyte was used as the active material (corresponding to a sulfur mass loading of ≈2 mg). 1.0 M lithium bistrifluoromethanesulfonylimide in 1,3-dioxolane (DOL) and 1,2-dimethoxyethane (DME) by 1:1 in volume with 0.1 M $LiNO_3$ additive was used as the electrolyte. The areas of all electrodes were ≈0.6 cm^2. The sulfur loading in the FLP-CNF and CNF electrodes was ≈3.3 mg cm^{-2}. The mass of pure CNF electrode and FLP-CNF electrode was ≈1 and ≈1.2 mg, respectively. For the tests in which the sulfur loading was increased to ≈5 mg cm^{-2}, ≈15 µL of 1 M lithium polysulfide (Li_2S_6) catholyte was used as the active material. All batteries were assembled in an Ar-filled glove box (MBraun Labstar). Arbin BT2000 battery instrument was used to perform charge/discharge testing within a voltage range of 1.5–2.8 V. Gamry Instruments potentiostat was used to perform cyclic voltammogram testing at room temperature.

Materials Characterization: Morphology observation was studied by SEM (Nova NanoSEM 430, 10 kV/5 kV), TEM (JEOL JEM 2010, 200 kV; FEI Titan G2 60–300 S/TEM, fitted with two CEOS Cs aberration correctors and monochrometer, 60 kV), and AFM (Nanoscope IIIa). EDS was used for collecting elemental signals and mapping. XRD patterns were collected by D-MAX/2400 with Cu Kα radiation. Optical microscopy was performed on Nikon ECLIPSE LV100D and Raman spectra were collected by LabRAM HR800 (632.8 nm He-Ne laser). Li_2S_6 solution (2 mL each, 5 mmol L^{-1}) was used for the ex situ adsorption measurement.

First Principles Calculations: Density functional theory (DFT) simulations using the open source software Quantum Espresso package was performed,[40] which utilizes by Perdew–Burke–Ernzerhof exchange–correlation functional within the generalized gradient approximation (GGA).[41] Generally, the GGA functional is a good choice for modeling systems involving covalent bonds, however, van der Waals forces are poorly captured in such simulations. Therefore, DFTD (D represents dispersion) technique to simulate the absorption of different Li_2S_x compounds on the phosphorene substrate was adopted. Simulations were conducted on 4 × 3 supercell (48 atoms) for monolayer phosphorene. A vacuum of 20 Å was used to avoid interactions between supercell images arising from periodicity. Kinetic energy and charge density cut-offs of 60 and 480 Ry were used for the wave functions and charge density, respectively, and the self-consistent field convergence criterion was set to 1×10^{-6} Ry. All the systems were relaxed using conjugate gradient minimization till the residual Hellmane-Feynman force on each atom was less than 10^{-3} Ry $Bohr^{-1}$. Initial structural relaxation was performed at the gamma *k*-point using the variable-cell relaxation procedure. The unit cell of the stable monolayer phosphorene had four P atoms, these atoms were arranged in puckered atomic planes. In the stable structure (shown in Supporting Information, Figure S11) each of the P atoms has two neighbors in the same plane and one neighbor in the other plane. The different lengths and bond angles were 2.26Å, 2.22Å and 103.5° and 96°, respectively. For binding energy computations, Brillouin zone integrations were performed over a Monkhorst-Pack grid with 4 × 4 × 1 *k*-points. Simulations to obtain estimates of binding energy of five molecules on α-phosphorene substrate were performed, these are Li_2S_6, Li_2S_4, Li_2S_3, Li_2S_2, and Li_2S. Li_2S was the final product of the discharge process and the initial reactant of the charging process.[42] The XCrysden package was used for visualization of the simulated results and charge densities.[43] Binding energies for Li_2S_x compounds were calculated as follows

$$E_b = E_{(Li_2S_x)} + E_{phosphorene} - E_{combine}, \qquad x = 1,2,3,4,6$$

where a positive value of E_b implies binding and larger binding energy would mean more favorable absorption.

Supporting Information

Supporting Information is available from the Wiley Online Library or from the author.

Acknowledgements

L.L. and L.C. contributed equally to this work. N.K. acknowledges funding support from the USA National Science Foundation (Awards Nos. 1234641, 1435783, 1510828, and 1608171) and the John A. Clark and Edward T. Crossan Endowed Chair Professorship at the Rensselaer Polytechnic Institute. C.V.S. acknowledges support from Natural Science and Engineering Research Council of Canada for funding, and Compute Canada Facilities SciNet and SharcNet for computational resources. W.R. and H.C. acknowledge funding supports from National Science Foundation of China (Grants Nos. 51325205, 51290273, and 51521091) and Chinese Academy of Sciences (Grant No. KGZD-EW-T06). The authors declare no competing financial interest.

Received: May 23, 2016
Revised: September 6, 2016
Published online:

[1] G. Zhou, F. Li, H.-M. Cheng, *Energy Environ. Sci.* **2014**, *7*, 1307.
[2] L. Li, Z. P. Wu, H. Sun, D. Chen, J. Gao, S. Suresh, P. Chow, C. V. Singh, N. Koratkar, *ACS Nano* **2015**, *9*, 11342.
[3] P. G. Bruce, S. A. Freunberger, L. J. Hardwick, J.-M. Tarascon, *Nat. Mater.* **2012**, *11*, 19.
[4] M.-Q. Zhao, Q. Zhang, J.-Q. Huang, G.-L. Tian, J.-Q. Nie, H.-J. Peng, F. Wei, *Nat. Commun.* **2014**, *5*, 3410.
[5] L. Ma, K. E. Hendrickson, S. Wei, L. A. Archer, *Nano Today* **2015**, *10*, 315.
[6] Y.-X. Yin, S. Xin, Y.-G. Guo, L.-J. Wan, *Angew. Chem. Int. Ed.* **2013**, *52*, 13186.
[7] Z. Li, J. Zhang, X. W. Lou, *Angew. Chem. Int. Ed.* **2015**, *54*, 12886.
[8] L. Li, Y. Yu, G. J. Ye, Q. Ge, X. Ou, H. Wu, D. Feng, X. H. Chen, Y. Zhang, *Nat. Nanotechnol.* **2014**, *9*, 372.
[9] M. Buscema, D. J. Groenendijk, S. I. Blanter, G. A. Steele, H. S. J. van der Zant, A. Castellanos-Gomez, *Nano Lett.* **2014**, *14*, 3347.
[10] H. Uk Lee, S. C. Lee, J. Won, B.-C. Son, S. Choi, Y. Kim, S. Y. Park, H.-S. Kim, Y.-C. Lee, J. Lee, *Sci. Rep.* **2015**, *5*, 8691.
[11] H. Liu, A. T. Neal, Z. Zhu, Z. Luo, X. Xu, D. Tománek, P. D. Ye, *ACS Nano* **2014**, *8*, 4033.
[12] J. Sun, H.-W. Lee, M. Pasta, H. Yuan, G. Zheng, Y. Sun, Y. Li, Y. Cui, *Nat. Nanotechnol.* **2015**, *10*, 980.
[13] L. Chen, G. Zhou, Z. Liu, X. Ma, J. Chen, Z. Zhang, X. Ma, F. Li, H.-M. Cheng, W. Ren, *Adv. Mater.* **2016**, *28*, 510.
[14] C. M. Park, H. J. Sohn, *Adv. Mater.* **2007**, *19*, 2465.
[15] P. W. Bridgman, *J. Am. Chem. Soc.* **1914**, *36*, 1344.
[16] Y. Maruyama, S. Suzuki, K. Kobayashi, S. Tanuma, *Physica B+C* **1981**, *105*, 99.
[17] S. Lange, P. Schmidt, T. Nilges, *Inorg.Chem.* **2007**, *46*, 4028.
[18] J. R. Brent, N. Savjani, E. A. Lewis, S. J. Haigh, D. J. Lewis, P. O'Brien, *Chem. Commun.* **2014**, *50*, 13338.
[19] S. P. Koenig, R. A. Doganov, H. Schmidt, A. H. Castro Neto, B. Özyilmaz, *Appl. Phys. Lett.* **2014**, *104*, 103106.
[20] D. Hanlon, C. Backes, E. Doherty, C. S. Cucinotta, N. C. Berner, C. Boland, K. Lee, A. Harvey, P. Lynch, Z. Gholamvand, S. Zhang, K. Wang, G. Moynihan, A. Pokle, Q. M. Ramasse, N. McEvoy, W. J. Blau, J. Wang, G. Abellan, F. Hauke, A. Hirsch, S. Sanvito, D. D. O/'Regan, G. S. Duesberg, V. Nicolosi, J. N. Coleman, *Nat. Commun.* **2015**, *6*, 8563.
[21] D.-W. Wang, Q. Zeng, G. Zhou, L. Yin, F. Li, H.-M. Cheng, I. R. Gentle, G. Q. M. Lu, *J. Mater. Chem. A* **2013**, *1*, 9382.
[22] X. Ji, K. T. Lee, L. F. Nazar, *Nat. Mater.* **2009**, *8*, 500.
[23] J. Guo, Y. Xu, C. Wang, *Nano Lett.* **2011**, *11*, 4288.
[24] G. Zhou, Y. Zhao, C. Zu, A. Manthiram, *Nano Energy* **2015**, *12*, 240.
[25] F. Maillard, A. Bonnefont, M. Chatenet, L. Guétaz, B. Doisneau-Cottignies, H. Roussel, U. Stimming, *Electrochim. Acta* **2007**, *53*, 811.
[26] X. Pu, G. Yang, C. Yu, *Adv. Mater.* **2014**, *26*, 7456.
[27] G. M. Zhou, L.-C. Yin, D.-W. Wang, L. Li, S. Pei, I. R. Gentle, F. Li, H.-M. Cheng, *ACS Nano* **2013**, *7*, 5367.
[28] T.-Z. Zhuang, J.-Q. Huang, H.-J. Peng, L.-Y. He, X.-B. Cheng, C.-M. Chen, Q. Zhang, *Small* **2016**, *12*, 381.
[29] G. Zheng, Y. Yang, J. J. Cha, S. S. Hong, Y. Cui, *Nano Lett.* **2011**, *11*, 4462.
[30] B. Wang, S. M. Alhassan, S. T. Pantelides, *Phys. Rev. Appl.* **2014**, *2*, 034004.
[31] Q. Zhang, Y. Wang, Z. W. Seh, Z. Fu, R. Zhang, Y. Cui, *Nano Lett.* **2015**, *15*, 3780.
[32] G. Zhou, E. Paek, G. S. Hwang, A. Manthiram, *Nat. Commun.* **2015**, *6*, 7760.
[33] H.-J. Peng, T.-Z. Hou, Q. Zhang, J.-Q. Huang, X.-B. Cheng, M.-Q. Guo, Z. Yuan, L.-Y. He, F. Wei, *Adv. Mater. Interfaces* **2014**, *1*, 1400227.
[34] J. Song, Z. Yu, M. L. Gordin, D. Wang, *Nano Lett.* **2016**, *16*, 864.
[35] Z. W. Seh, J. H. Yu, W. Li, P.-C. Hsu, H. Wang, Y. Sun, H. Yao, Q. Zhang, Y. Cui, *Nat. Commun.* **2014**, *5*, 5017.
[36] X. Tao, J. Wang, C. Liu, H. Wang, H. Yao, G. Zheng, Z. W. Seh, Q. Cai, W. Li, G. Zhou, C. Zu, Y. Cui, *Nat. Commun.* **2016**, *7*, 11203.
[37] Q. Pang, L. F. Nazar, *ACS Nano* **2016**, *10*, 4111.
[38] Z. Cui, C. Zu, W. Zhou, A. Manthiram, J. B. Goodenough, *Adv. Mater.* **2016**, *28*, 6926.
[39] J. Liu, W. Li, L. Duan, X. Li, L. Ji, Z. Geng, K. Huang, L. Lu, L. Zhou, Z. Liu, W. Chen, L. Liu, S. Feng, Y. Zhang, *Nano Lett.* **2015**, *15*, 5137.
[40] J. P. Perdew, K. Burke, M. Ernzerhof, *Phys. Rev. Lett.* **1996**, *77*, 3865.
[41] H. J. Monkhorst, J. D. Pack, *Phys. Rev. B* **1976**, *13*, 5188.
[42] R. Xu, I. Belharouak, J. C. M. Li, X. Zhang, I. Bloom, J. Bareño, *Adv. Energy Mater.* **2013**, *3*, 833.
[43] A. Kokalj, *Comput. Mater. Sci.* **2003**, *28*, 155.